Dissolution Processes at TTF−TCNQ Single-Crystal Electrodes: A Dynamic *in Situ* Electrochemical Scanning Tunneling Microscopy Study

P. N. Bartlett* and X. Q. Tong

Department of Chemistry, University of Southampton, Southampton SO17 1BJ, UK

Received: May 20, 1997; In Final Form: August 2, 1997⊗

Surface transformations occurring at the (001) face of tetrathiafulvalene−tetracyanoquinodimethane (TTF−TCNQ) single crystals in aqueous solution have been studied by in situ electrochemical scanning tunneling microscopy (ECSTM) both at equilibrium and under electrochemically driven dissolution conditions. The TTF and TCNQ molecules present in segregated molecular stacks at the crystal surface have been resolved at atomic resolution in different solutions and at various applied electrochemical potentials. The images display the same atomic features seen by STM in air. Surface features and defects on the molecular scale, such as flat terraces, ledges of monomolecular height, kinks due to molecules of reduced coordination at the ends of molecular stacks, and vacancies within stacks due to missing molecules, have been seen to play a crucial part in the dissolution processes at these electrodes. Observations of interfacial dissolution and electrochemical reactions under controlled potential by dynamic ECSTM imaging at a molecular level suggest that the kinetics of these processes are dependent on the orientations of surface ledges and kink density in relation to the crystallographic axes of the crystal. The mechanism of dissolution is found to involve preferential removal of molecules along the molecular stacks in a molecule-by-molecule sequence occurring at the kink sites. These phenomena can be rationalized in terms of their relation to the anisotropic properties of this material which arise from strong intermolecular bonding and partial charge transfer between the molecules within the molecular stacks but with weaker interactions between stacks. Effects caused by the proximity of the STM tip leading to local modification of the interfacial electrochemistry have also been observed and are discussed.

Introduction

Low-dimensional organic systems have recently been the subject of studies by scanning tunneling microscopy (STM) and atomic force microscopy (AFM), since these scanning probe techniques have been recognized as suitable and powerful tools to provide nanoscale information about the topography and structure of the surfaces of these materials. Among these materials, due to its relatively high electrical conductivity and interesting electronic properties, the conducting organic salt tetrathiafulvalene−tetracyanoquinodimethane (TTF−TCNQ) is probably the most extensively examined so far, particularly by STM in ambient air.[1−6] TTF−TCNQ is composed of segregated parallel stacks of donor TTF molecules and acceptor TCNQ molecules. There is partial charge transfer from the highest occupied molecular orbitals (HOMO) of TTF to the lowest unoccupied molecular orbitals (LUMO) of TCNQ, leading to the transfer of approximately one electron for every two TTF molecules. This results in a quasi-one-dimensional solid-state structure in which the highest conductivity is along the stacking direction. It is the HOMO orbitals of TTF and LUMO orbitals of TCNQ that contribute to the tunneling current and hence the image contrast in the STM. Although high-resolution STM images identifying individual molecules have been obtained for both single-crystal TTF−TCNQ[1−3] and TTF−TCNQ thin films deposited on well-defined substrates,[4−6] certain anomalies exist in the reported molecular images representing the *ab* crystal face of TTF−TCNQ, and interpretations of observed image differences remain controversial.[3,6]

The good solid-state conductivity and charge-transfer characteristics of the TTF−TCNQ have, on the other hand, led to a growing interest in its electrochemical properties as an electrode material. The cyclic voltammetric behavior of TTF−TCNQ in various aqueous media was first investigated by Jaeger and Bard.[7] They found that TTF−TCNQ electrodes in various aqueous supporting electrolyte solutions exhibited a wide potential region of electrode stability (generally from −0.2 to +0.5 V vs SCE) over which no current peaks could be seen. Outside this stable potential region the decomposition of the electrode occurs by either oxidation or reduction of the electrode components. The particular characteristics of these electrodes have also generated further interest in their potential applications in biosensor devices in which materials such as TTF−TCNQ have been used as electrodes in aqueous solutions for oxidation of enzymes at low overpotential. Substantial electrochemical measurements have been carried out to investigate the performance of TTF−TCNQ enzyme electrodes, and some possible reaction mechanisms involving mediation by the electrode constituents have been proposed.[8,9] However, little is known about the nature of the TTF−TCNQ electrode/electrolyte interface although this is clearly crucial to the electrochemical processes. The understanding of the chemical, electronic, and topographic structure of the electrode surface plays an important role in any understanding of the mechanisms of interfacial reactions at these electrodes. Further advances in this regard require characterization, at a microscopic level, of surface defects and topographic features, such as terraces, ledges, and kinks, which may relate directly to the observed electrochemical reactivity and kinetics. In situ electrochemical STM and AFM now allow changes of interfacial morphology, structure, and the distribution of surface features to be monitored dynamically in solution under electrochemical control at micron to nanometer scales.

The electrochemical processes occurring at the TTF−TCNQ electrode are not only dependent on the applied potential and

---

TTF−TCNQ Single-Crystal Electrodes

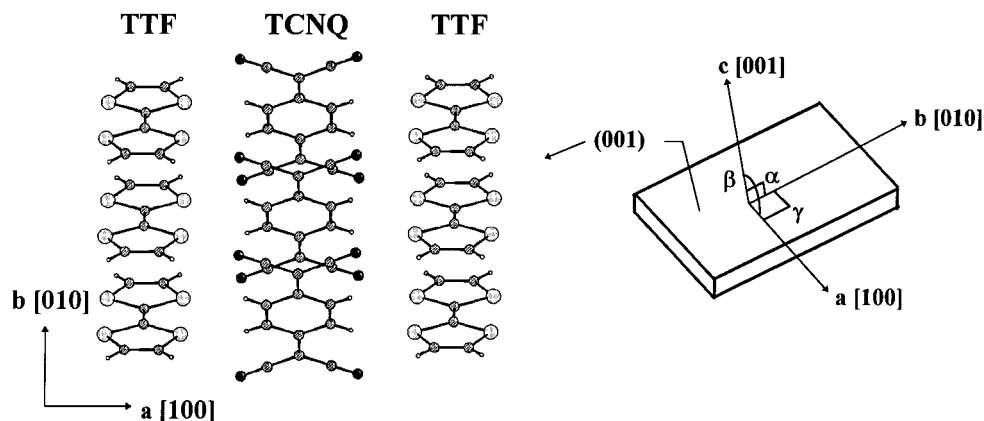*J. Phys. Chem. B, Vol. 101, No. 42, 1997* **8541**

Figure 1. Diagram of the TTF−TCNQ single-crystal sample showing the main crystal axes and the molecular structure of the largest habit plane {001} which was the one used in the in situ ECSTM imaging.

the electrolyte, but they also depend on the electrode history. It is therefore our primary interest to investigate different surface evolution processes occurring in aqueous solutions under conditions of well-defined and controlled electrode potential. The present work reports dissolution phenomena at TTF−TCNQ single-crystal electrode surfaces. The topography of the dissolving surface has been imaged in situ and in real time at both equilibrium and nonequilibrium potentials, using both potentiostatic and potentiodynamic techniques. The atomically resolved images that we have obtained in situ at TTF−TCNQ electrode surfaces have helped us to develop a better understanding of the relationship among the intermolecular interactions, the crystal surface structure, and the mechanism of dissolution. It is widely acknowledged that surface terraces, ledges, kinks, and other defects play an important role in the dissolution of single crystals. Our work attempts to provide a study of the detailed dynamics of the changes in these features at the molecular level during dissolution. In addition, different dissolution phenomena at different electrode potentials have been observed and are interpreted in terms of variations of the undersaturation at the local surface caused by electrochemical effects, some of which are induced by the STM tip itself.

Experimental Section

Crystal Samples. TTF−TCNQ single crystals were grown by slow diffusion synthesis.[10,11] They were washed with cold HPLC grade acetonitrile (Sigma−Aldrich) and then diethyl ether (BDH). The crystals were indexed by an X-ray diffractometer. The lattice parameters were consistent with literature values (a = 12.298 Å, b = 3.819 Å, c = 18.468 Å, $\alpha = \gamma = 90°$, β = 104.46°). The largest flat crystal surface was always the ab or (001) face and the longest crystal dimension the stack direction along b or [010] (see Figure 1).

Electrolyte Solutions. Aqueous solutions (0.01 M) of LiCl (Fisons) or NaCl (Aldrich) were used in all experiments. TTF−TCNQ electrochemistry has been studied previously in both electrolytes,[7,11] although the concentrations used in the present work are somewhat lower to ensure compatibility with the ECSTM technique. In experiments using NaCl solutions the electrolyte was saturated with TTF and TCNQ before use to reduce the initial rate of dissolution.

ECSTM. A TopoMetrix TMX2010 scanning tunneling microscope with a 1 μm tube scanner and a conventional bipotentiostat were used for in situ ECSTM experiments. A homemade electrochemical cell was constructed specially to meet the needs of in situ ECSTM imaging of TTF−TCNQ crystals resulting from the small dimensions of the crystals (typically 0.7 × 0.2 × 0.03 mm). Figure 2 is a schematic representation of the cell. It is designed to allow easy mounting
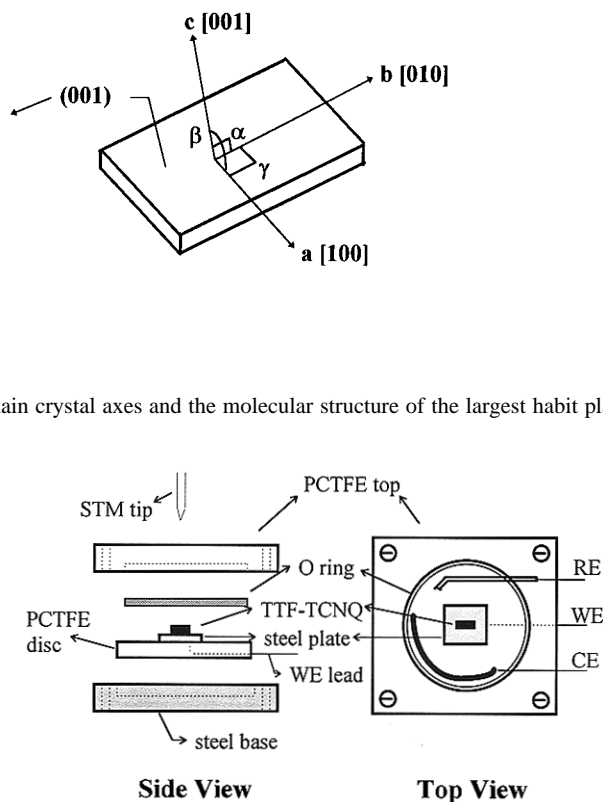

Side View   **Top View**

Figure 2. Diagram of the specially constructed electrochemical cell used for in situ ECSTM studies of TTF−TCNQ single-crystal electrodes of small dimension.

and replacement of the sample while still allowing the location of the STM tip on the sample at chosen positions using the TopoMetrix video camera system. As shown in Figure 2, the sample supporting base is composed of a small flat steel plate glued firmly with nonconducting epoxy onto a PCTFE disk. One of the largest crystal faces of the sample was fixed onto the steel plate using silver-loaded paint (Agar). The crystal edges, the silver paint, and the whole steel plate were then masked by nail varnish so that only the largest crystal face was exposed to the electrolyte. The mounted crystal was then assembled together with the remaining parts of the cell. Because of the difficulties in handling such small and fragile crystal samples, cleaning the sample and cell is difficult, and it is possible that some contaminants may be present in the system. Small Ag/AgCl/LiCl (1 M) or Ag/AgCl/NaCl (1 M) reference electrodes (for use in the 0.01 M LiCl or 0.01 M NaCl solutions, respectively) for the ECSTM cell were made in-house. The reference electrodes were routinely calibrated against a saturated calomel electrode (SCE), and all potentials are reported with respect to SCE. A Pt wire was used as the counter electrode. STM tips were made from $Pt_{80}Ir_{20}$ wires etched by ac current in 2 M $CaCl_2$ solution and then coated with Apiezon wax. The faradaic current at the tip during the experiments was below 50 pA.

The etching of surface layers in the STM and AFM of layered molecular crystals due to tip−surface interactions during imaging has been commonly observed.[12,13] Optimal imaging condition is therefore important to minimize the interactions in order to extract true surface information.[12] In our experiments all the imaging processes started with a small tunneling current I_t (normally 0.5 nA), a relatively high bias voltage E_b (usually 0.2 V), and a relatively slow scan rate (typically 2−4 times the scan size per second for relatively large scale images). I_t was gradually increased only when better resolved images (e.g.,
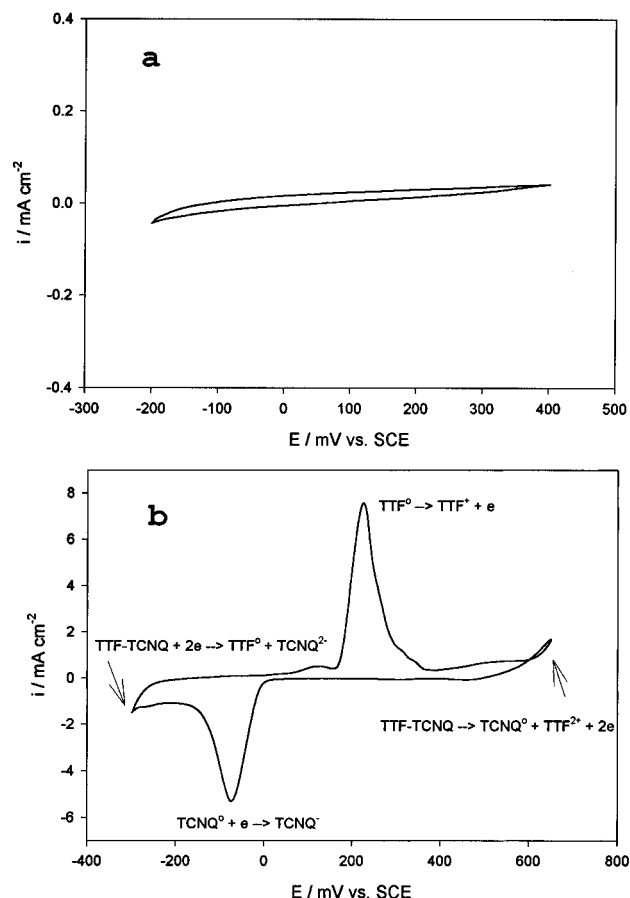
Figure 3. Cyclic voltammograms of a TTF−TCNQ single-crystal electrode in 0.01 M LiCl recorded at 20 mV s^{-1} showing the electrochemical behavior in the stable potential region (curve a) and when both limits of the stable region are exceeded (curve b).

atomic resolution) were acquired. A fast scan rate was used only when it was necessary to extract the true dissolution data due to a fast dissolution rate[13] or to thermal drift. E_b variation was sometimes required to allow control of the tip potential E_t or sample potential E_s. To eliminate the confusion between the tip-induced surface etching and the true surface dissolution process in solution, we carried out comparison of images obtained in air and in solution under the same imaging condition to confirm that what we had observed was mainly due to the dissolution process. We also performed such confirmation in situ by zooming out of the scanned area.

Results

Electrochemical Characteristics. Figure 3 shows the typical electrochemical behavior of TTF−TCNQ single-crystal electrodes in aqueous 0.01 M LiCl solution. Between about −0.2 and +0.4 V (Figure 3a) the voltammetry is featureless with only nonfaradaic capacitive currents observed. By chronoamperometry using ferricyanide[8a] we estimate the exposed electrode area to be 0.01 cm^2, which agrees well with our best estimate of the exposed area of the crystal. In 0.01 M LiCl the open circuit potential, E_0, for the crystal was found to lie between −50 and +30 mV.

If the electrode potential is taken to a value more negative than about −0.2 V, the TTF−TCNQ is reduced to give TTF^0 and TCNQ^{2-} [7]

$$TTF-TCNQ + 2e^- \rightarrow TTF^0 + TCNQ^{2-} \qquad (1)$$

Since TTF^0 is insoluble, it remains on the surface of the electrode. In chloride solutions the insoluble TTF^0 is oxidized

and converted to TTFCl when the potential is swept anodically.

$$TTF^0 + Cl^-(aq) \rightarrow TTFCl + e^- \qquad (2)$$

As shown in Figure 3b, this oxidation process occurs at about 0.24 V in 0.01 M LiCl. This is shifted approximately 120 mV anodic of the corresponding potential reported by Jaeger and Bard[7] for the same process in 1 M LiCl because the chloride concentration is 2 orders of magnitude lower in our experiments.

Thus, there is good agreement between the voltammetry on the (001) face of our single-crystal electrodes and the voltammetry reported by Jaeger and Bard[7] for polycrystalline compressed pellet samples. However, in our experiments we do not see evidence for the subsequent reduction of the TTFCl to TTF^0 on the electrode surface. We attribute this difference to the fact that the amounts of TTFCl formed in our experiments are low and the fact that the chloride concentration is lower so that the TTFCl is sufficiently soluble to dissolve from the electrode surface during the potential scan.

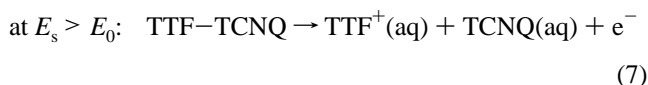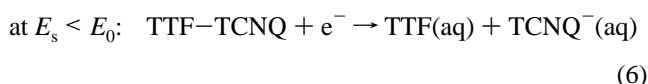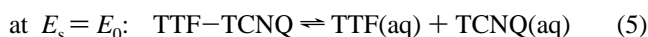If the electrode is taken to potentials more positive than about 0.4 V, the TTF−TCNQ is oxidized, giving

$$TTF-TCNQ \rightarrow TTF^{2+} + TCNQ^0 + 2e^- \qquad (3)$$
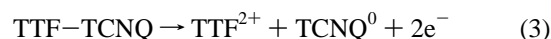
During the subsequent cathodic potential scan, the insoluble TCNQ^0 is reduced to TCNQ$^-$ (see Figure 3b)

$$TCNQ^0 + e^- \rightarrow TCNQ^- \qquad (4)$$

In the LiCl solution TCNQ$^-$ is soluble and is lost from the electrode surface. In contrast, in NaCl solution insoluble NaTCNQ salt is deposited on the electrode surface.[11]

When the electrode potential, E_s, is set within the region between −0.2 and 0.4 V, either at the equilibrium potential, E_0, or positive or negative of E_0, the processes expected to occur at the electrode surface are

at $E_s = E_0$: $TTF-TCNQ \rightleftharpoons TTF(aq) + TCNQ(aq)$ (5)

at $E_s < E_0$: $TTF-TCNQ + e^- \rightarrow TTF(aq) + TCNQ^-(aq)$

(6)

at $E_s > E_0$: $TTF-TCNQ \rightarrow TTF^+(aq) + TCNQ(aq) + e^-$

(7)

where to distinguish them from TTF^0 and TCNQ^0 at the electrode surface TTF(aq) and TCNQ(aq) in (5)−(7) represent the neutral species dissolved in the solution. As indicated by (6) and (7), the saturation at the interface can be modified and give rise to the dissolution at nonequilibrium potentials. Dissolution can also take place at E_0 if the solution is not saturated with the electrode components, as is the case for the LiCl solution used here. Even when the contacting solution is presaturated with the electrode components dissolution can still occur due to undersaturation caused by temperature changes or other local factors. We return to this point below.

Surface Evolution within the Stable Potential Region: A Potentiostatic ECSTM Study. *Dissolution at the Equilibrium Potential.* We always observed some dissolution of the electrode even in TTF and TCNQ saturated NaCl solution at E_0. The dissolution rate was found to be faster at the beginning of the experiment after the STM tip and the sample were aligned and the electrochemical cell was set up. The longer the system was allowed to rest at equilibrium, the slower the rate of dissolution becomes. This is probably due to an initial temperature rise in the cell produced by the light source for the video camera system used to help align the tip on the very small
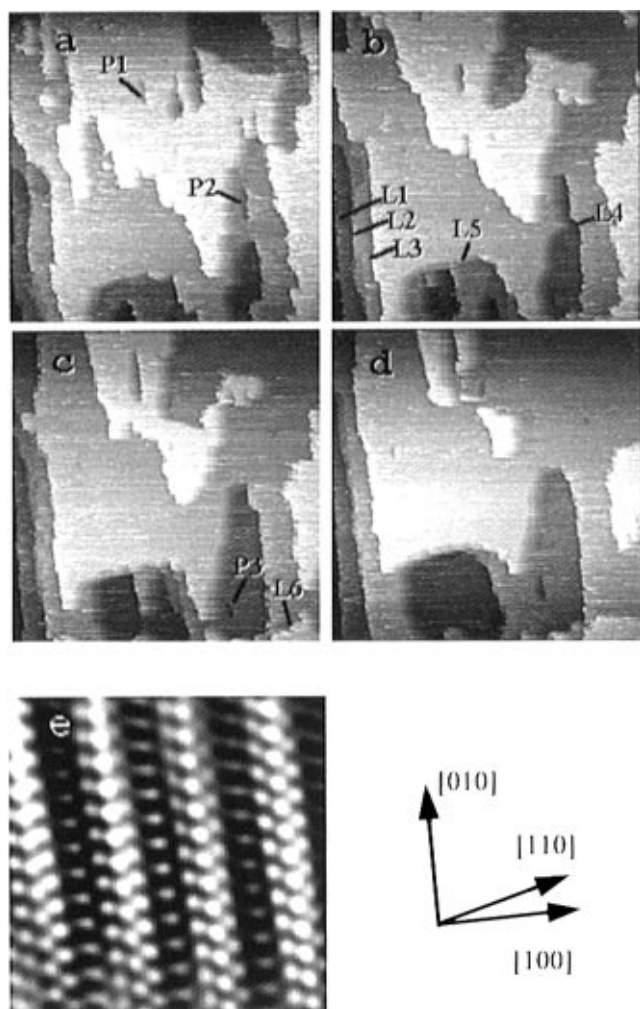
Figure 4. Images of the TTF−TCNQ surface with E_b = 200 mV, I_t = 0.5 nA, at the equilibrium potential (E_s = −40 mV) in 0.01 M NaCl saturated with TTF and TCNQ: (a)−(d) sequence of raw topographic images (455.5 × 455.5 nm) obtained in a continuous sequence at a scan rate of 1 μm s^{-1}; the contrast in the images corresponds to a vertical range of zero to 6 nm. (e) TTF−TCNQ molecular image (4.5 × 4.5 nm) after FFT low pass filtering obtained in constant height mode at a scan rate of 300 nm s^{-1}. The row formed by the triple spots represents the TCNQ stack, and the row with the single spots represents the TTF stack; the stacks lie along the ⟨010⟩ crystallographic axis as indicated.

sample. Such a temperature rise would promote initial dissolution. A similar finding has been reported in a study of the dissolution of KBr single crystals in saturated solution by an integrated electrochemical/AFM probe technique.[14] We found that imaging dissolution in the initial stages was difficult because the surface feature in the images, such as monomolecular steps, could move out of the image frame between successive scans. However, by allowing sufficient time for the system to stabilize after assembly in the ECSTM (typically 30 min), the dissolution rate decreased and dynamic imaging was possible. The images in Figure 4 were obtained under such relatively stable temperature conditions.

Figure 4a−d shows four unfiltered in situ ECSTM topographic images captured in succession; each image took just under 3 min to complete. The large flat terraces, ledges of different orientation, and the numerous kinks can clearly be seen. These are common features observed for slow dissolution processes at the TTF−TCNQ interface. The terraces are of monomolecular height, 9.8 ± 0.5 Å, corresponding to about one-half of the *c* lattice parameter. Figure 4e is a current image at atomic resolution obtained on a flat terrace area. The parallel triplet rows correspond to the TCNQ molecular stacks and the single spot rows to the TTF molecular stacks along ⟨010⟩. The

unit cell *a* and *b* parameters are consistent with reported values. The middle spot in the triplet of TCNQ appears to be the highest one; this has been observed by others[1,5,6,12] by STM in air. From Figure 4e, the crystal axes for the images of Figure 4a−d can be inferred.

Figure 4 provides key information on the progress of dissolution by the movement of the monomolecular ledges of various orientations and at different rates. Let us look first at the three parallel ledges (L1, L2, and L3) close to the image frame on the left-hand side. The lower parts of these ledges are nearly parallel to ⟨010⟩, the molecular stack direction. At the beginning (Figure 4a,b) the upper parts of these ledges gradually retreat, generally in the [100] direction by removal of material in the ⟨010⟩ direction. In comparison, the lower parts of the ledges retreat very slowly. While initially some kinks are visible in the lower parts of the ledges these gradually disappear, and the ledges are "straightened" as dissolution proceeds. Similar ledge "straightening" effects can be seen for other ledge sites, such as L4 and L5. In the case of ledge L5, the ledge is gradually straightened so that the majority of L5 is almost parallel to ⟨100⟩. By comparison, in the later stages (Figure 4c,d), the advancement of L5 slows down. At the same time, ledges of other orientations move across the surface in a similar manner with different, but relatively higher, rates. Localized dissolution and growth leading to ledge reshaping can be seen for L6. Dissolution also occurs at lower-lying layers at the same time. Pit initiation at P1 and P2 results in local dissolution beginning in the middle of terraces.

To observe the dissolution process at a molecular level, we zoomed in our images at various ledge sites to obtain molecularly resolved images of the ledges and kinks, as shown in Figures 5 and 6. Each image in Figure 5 or 6 took 11 s to acquire. Imaging with the same instrumental parameters on a distinguishable area was carried out many times beforehand to confirm that the scan rate used was faster than the rate of movement of the ledges at these image sizes. Thus, in these experiments the distortion in the images caused by movement of the ledge during the imaging is negligible. Although the images have some noise associated with surface species and contaminants, ledges of two different orientations containing different kink features can be clearly seen in Figure 5. These kinks are due to different numbers of missing molecules at the ends of each molecular row and are therefore referred to as molecular kinks. One of the stacks, marked by the arrowhead in Figure 5a, looks like a broken stack (or double-kink site) as a result of missing molecules in the middle of the stack. The distance between two neighboring molecular kinks along the stacks in Figure 5a is larger than that in Figure 5b, which seems to have almost equally spaced kinks. The orientation of the ledge in Figure 5b is very close to ⟨110⟩. It can be envisaged that, for a fixed distance, the number of kinks on the ledge in Figure 5b will be greater than that on the ledge in Figure 5a. Figure 6 is a sequence of images captured successively on the same area, each taking 11 s to complete. A diagonally oriented ledge (indicated by the broken line) appears in the lower right corner of Figure 6a, and its advance is recorded in Figure 6b,c. Two monomolecular ledges appear to be present in Figure 6b, and they begin to merge in Figure 6c. This provides direct evidence that ledge movement is the result of molecular detachment from the ends of the stacks at the kink sites.

Dissolution at Nonequilibrium Potentials. The undersaturation at the TTF−TCNQ surface can be changed by changing the electrode potential, E_s, within the stable region. We have imaged the same selected surface area at potentials both cathodic and anodic of the equilibrium potential, E_0, to compare dissolution under the different conditions. Figure 7 provides a
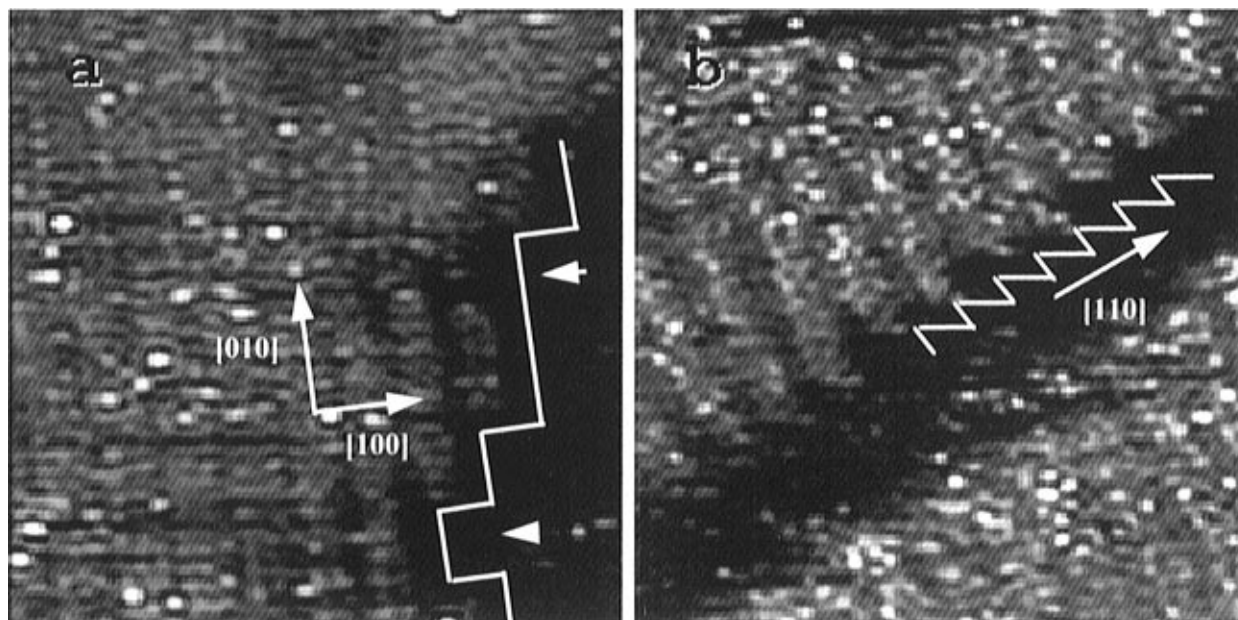
Figure 5. Current images (after FFT low pass filtering) of TTF−TCNQ surface ledges and kinks, obtained with $E_b = 200$ mV under the same electrochemical conditions as given in Figure 4: (a) 10×10 nm, $I_t = 1.5$ nA, and a scan rate of 300 nm s^{-1}; (b) 10.2×10.2 nm, $I_t = 3.5$ nA, and a scan rate 200 nm s^{-1}. The white lines are drawn to indicate the positions of the ledges and kinks.
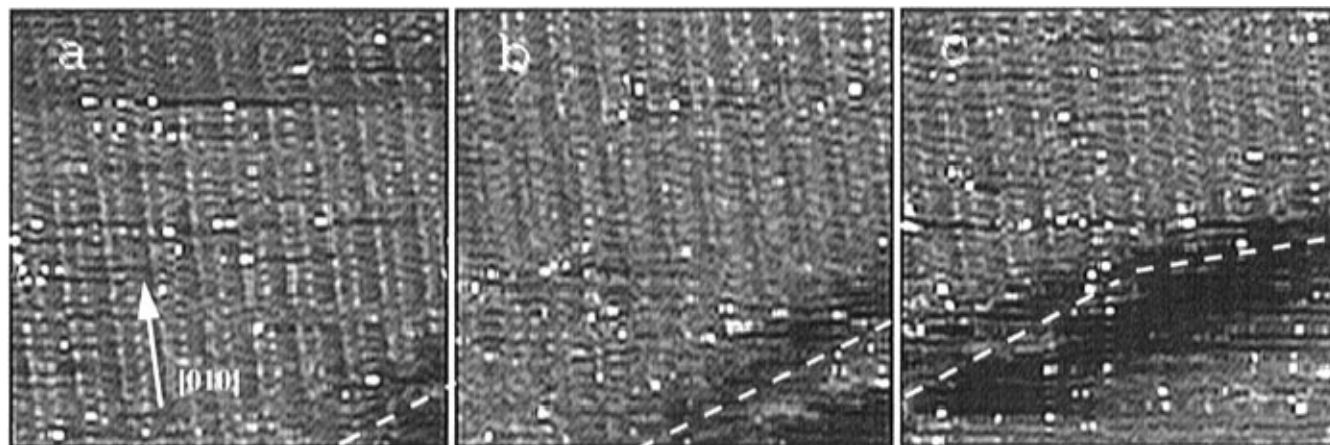

Figure 6. Successive 10×10 nm current images (after FFT low pass filtering) of dynamic surface ledge movement at the TTF−TCNQ electrode under the same electrochemical conditions as given in Figure 4, with $I_t = 3.5$ nA, $E_b = 200$ mV, and a scan rate of 300 nm s^{-1}.

comparison of the dissolution characteristics at the different potentials. It comprises four sequences, each of three images captured in succession. Each image took 80 s to acquire. Between each sequence, the STM tip remained engaged (but not scanning) while E_s was changed to the new value by slowly ramping the potentials of both the sample, E_s, and the tip, E_t, in parallel so that the potential difference between the two, E_b, was kept constant. For Figure 7 the equilibrium potential, E_0, was 10 mV, and the imaging conditions I_t, E_b, and the scan rate were kept constant for all images in the first three sequences. However, for the last sequence the sign of E_b was reversed in order to reduce E_t as discussed below. Note that image drift within each sequence is negligible but that slight drifts along the y-axis occurred between sequences. We attribute this to nonlinearities of the scanner.

In general, the majority of surface ledges in Figure 7 are again oriented almost parallel to the stack direction $\langle 010 \rangle$ and move toward $\langle 100 \rangle$. Sequence 1 in Figure 7 shows gradual dissolution at $E_s < E_0$ ($E_s = -140$ mV, $E_t = 60$ mV) where undersaturation due to the cathodic reduction of TCNQ according to eq 6 can be expected. As with the observations in Figure 4, $\langle 010 \rangle$ ledges shift very slowly while ledges with other orientations move across the surface more rapidly. Most of the $\langle 010 \rangle$ ledges merge closely together, forming multiple ledges which hardly move.

Dissolution can also be seen to occur vertically at locations marked by P1 (probably along the crystal c axis or [00$\bar{1}$]) at a comparable rate relative to the lateral dissolution. In comparison, at the equilibrium potential ($E_s = E_0$, $E_s = 10$ mV, $E_t = 210$ mV) sequence 2 shows that there is only a very slight change in the surface, indicating a much smaller undersaturation and lower dissolution rate for the equilibrium process given by eq 5. In this sequence we can see a pit nucleate at P2 in the second image and then grow both laterally and vertically in the third image. Due to the slight image drift, some features not seen in sequence 1 appear at the top of the frame in sequence 2. The third sequence was obtained at $E_s > E_0$ ($E_s = 210$ mV, $E_t = 410$ mV) and shows quite different dissolution features from the previous two. In this case there is a clear indication of reduction in terrace width resulting from faster ledge movement across the surface. The lateral dissolution rate is obviously higher than the vertical one, resulting in the promotion of movement of a large number of ledges along $\langle 100 \rangle$ so that some of the multiple ledges start to split into monomolecular ledges, and the depth features due to the prior vertical dissolution gradually become shallow and finally disappear. Although the expected anodic reaction of TTF oxidation, eq 7, will cause undersaturation, and although one could argue that the much larger dissolution rate that we observe at the cathodic potential
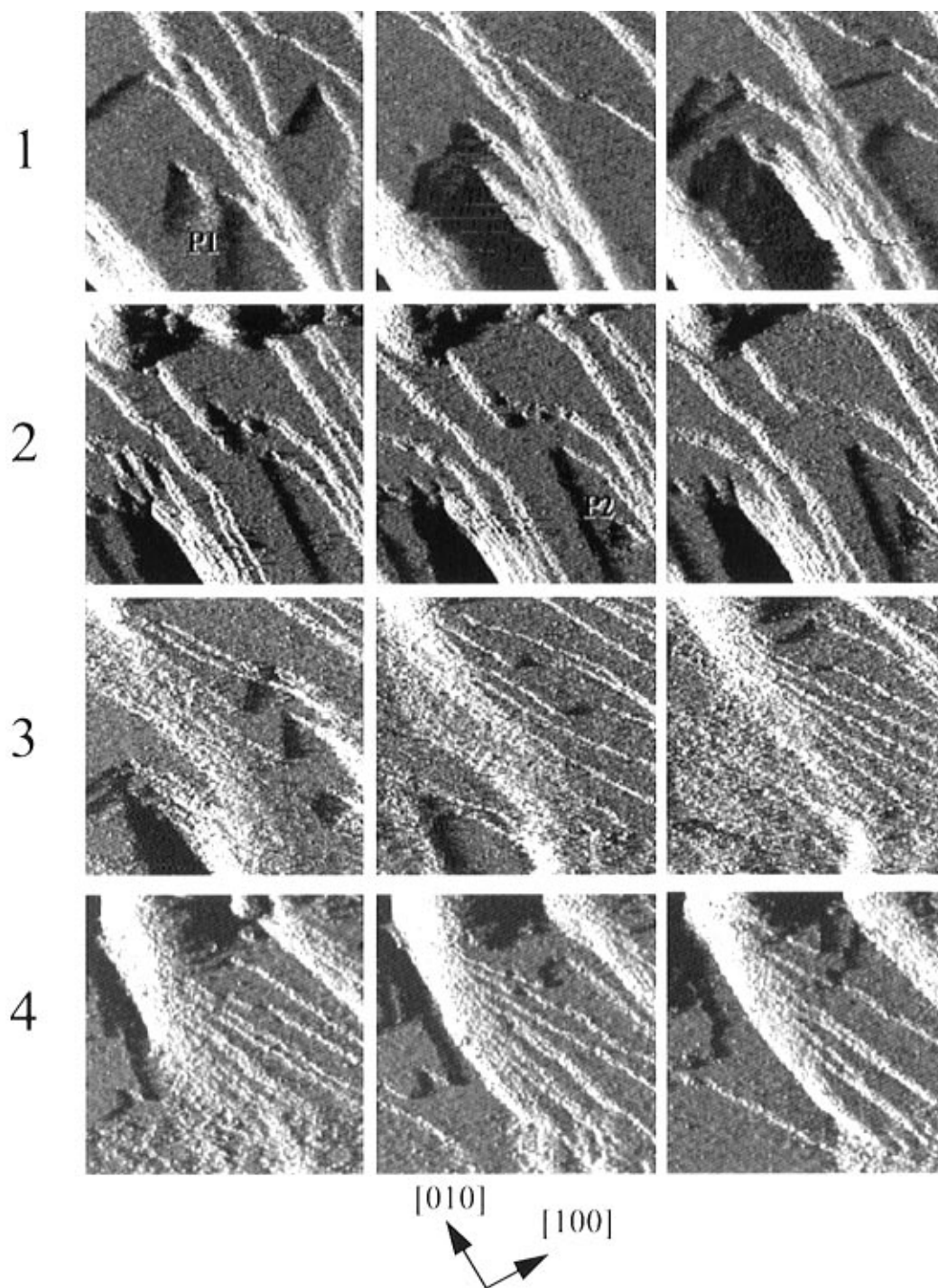
Figure 7. Four sequences of shaded topographic images (495.5 × 495.5 nm, $I_t = 0.5$ nA, scan rate 2 μm s^{-1}), each sequence consisting of three images captured in succession, of surface dissolution in 0.01 M NaCl at various sample and tip potentials: (1) $E_s = -140$ mV, $E_t = 60$ mV; (2) $E_s = E_0 = 10$ mV, $E_t = 210$ mV; (3) $E_s = 210$ mV, $E_t = 410$ mV; (4) $E_s = 210$ mV, $E_t = 10$ mV.

could be the result of the difference in the overpotential employed for sequences 1 and 3, this is not borne out by sequence 4. In sequence 4 E_s was kept the same as for sequence 3 ($E_s = 210$ mV), but the tip potential, E_t, was reduced to 10 mV so that the sign of the tip−substrate potential difference was reversed while keeping the tip to sample distance unchanged ($E_b = -200$ mV). With these changes in imaging conditions sequence 4 clearly shows dissolution features very similar to those of sequences 1 and 2, typical of a more slowly dissolving surface. Therefore, we conclude that the difference in the applied overpotential cannot be solely responsible for the rapid lateral dissolution observed in sequence 3; rather, we believe that there is tip-induced dissolution occurring in sequence 3. We return to this point below.

Surface Evolution outside the Stable Potential Region: A Potentiodynamic ECSTM Study. Alternating imaging with sample potential sweeps has been performed to obtain information about the surface changes that occur when the crystals are taken to potentials outside the stable region where reduction or oxidation of the electrode components occurs as described by eq 1 or 4. During the cyclic potential sweep the imaging tip was withdrawn a fixed distance and then reengaged at E_0 onto the same selected area for imaging after the end of the electrode potential sweep. Typical results are shown in Figure 8.

In general, under these conditions we observe surface changes similar to those described above for dissolution, but on a scale and at a rate that is substantially larger. As the number of electrode potential sweeps is increased, the surface becomes
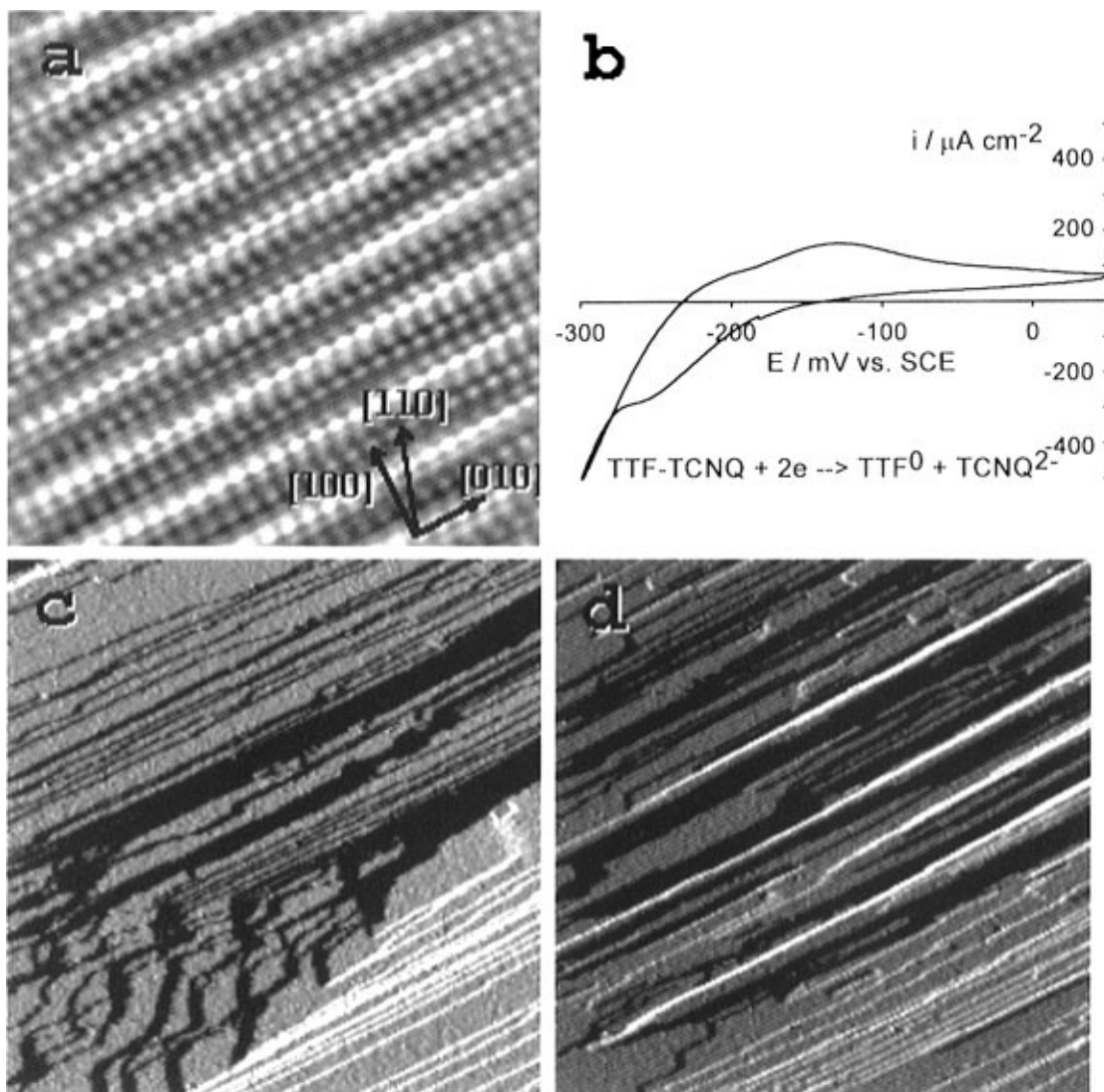
Figure 8. Shaded topographic images ($E_b = -70$ mV) obtained at the equilibrium potential in 0.01 M LiCl solution: (a) 8×8 nm atomic resolution of the initial surface obtained before potential sweep with $I_t = 5$ nA and a scan rate of 250 nm s^{-1}; (c, d) a selected surface area (635 $\times$ 635 nm, $I_t = 1$ nA, and a scan rate of 900 nm s^{-1}) after electrode potential sweeps between -300 and 50 mV at 20 mV s^{-1}. A typical voltammogram of such a sweep is shown in (b).

dominated by narrow (001) terraces bounded by $\langle 010 \rangle$ ledges; see Figure 8c,d. The typical course of such changes can be seen by comparison of parts c and d of Figure 8. The orientation of the crystal was established by imaging at atomic resolution on a flat terrace region and is shown in Figure 8a. A number of ledges orientated close to $\langle 110 \rangle$ in the lower left part of Figure 8c disappeared following cathodic reduction of the crystal according to eq 1 during two cycles of the electrode potential between -300 and $+50$ mV at 20 mV s^{-1}; Figure 8b shows the corresponding voltammogram for the electrode. In Figure 8d there is an obvious increase in the frequency of (001) terraces and $\langle 010 \rangle$ ledges. These results suggest that ledge and kink sites also play an important role in surface reduction or oxidation reactions. Generally, the ledges were seen to shift constantly and merge. The shift of the ledges was generally slowed when they merged, forming a highly faceted surface with multiple steps. Dissolution also occurred simultaneously into the crystal surface, [00$\bar{1}$] direction, at some locations producing valleys. As a result, the electrode surface became much rougher after these potential cycles as compared to that resulting from dissolution process occurring within the stable region. This is accompanied by a gradual decrease in the surface conductivity due to the coverage of the surface by insulating TTF^0 or TCNQ^0. Because of these complications, high-resolution molecular

images of the surface after this type of dissolution could not be obtained although numerous attempts were made.

Discussion

Starting from the molecular stack structure of TTF$-$TCNQ, we can deduced a simplified relationship between the ledge orientation and the density of molecular kinks at that ledge. As shown in Figure 9, we denote a ledge having a chevron angle θ against the $\langle 010 \rangle$ molecular axis as a θ ledge and the interkink distance along $\langle 010 \rangle$ as $k_{\langle 010 \rangle}$. Then a ledge with a small value of θ will have a large average value of $k_{\langle 010 \rangle}$, and as θ increases, that is, as the orientation of the ledge moves more toward $\langle 100 \rangle$, the average value of $k_{\langle 010 \rangle}$ decreases. If we define the density of molecular kinks as the number of molecular kinks on unit length of the ledge, then this molecular kink density will have a maximum value when the ledge is oriented close to the $\langle 110 \rangle$ axis where $k_{\langle 010 \rangle}$ will have a value close to the difference in the molecular stack spacing between the two neighboring rows. There are two extreme cases when the kink density will be zero: either when $\theta = 0°$ for $\langle 010 \rangle$ ledges where $k_{\langle 010 \rangle}$ will be very large or when $\theta = 90°$ for $\langle 100 \rangle$ ledges where $k_{\langle 010 \rangle}$ is zero. Ledges with a high concentration of molecular kinks are associated with high index crystal planes and are thermodynamically unstable because of their higher surface energies.[15]
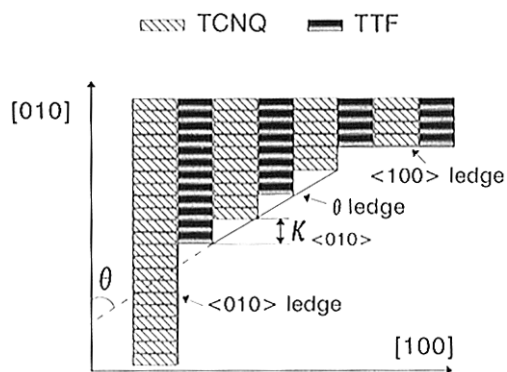
TTF−TCNQ Single-Crystal Electrodes

J. Phys. Chem. B, Vol. 101, No. 42, 1997 **8547**

Figure 9. Schematic representation of molecular kinks and ledge orientations with respect to crystallographic indices on the (001) face of TTF−TCNQ.

The coordination number of the molecules at kinks is reduced, and they are therefore easily detached from the terrace during dissolution, leading to preferential dissolution in the stacking direction ⟨010⟩. Therefore, the dissolution mechanism of TTF− TCNQ can generally be described as the molecule-by-molecule detachment at the molecular stacks along ⟨010⟩ and stack-by-stack removal of TTF and TCNQ molecules along the perpendicular axis ⟨100⟩. The rate of movement of a ledge is generally proportional to its kink density.

It is now easy to understand the observations in Figure 4a− d. The lower parts of ledges L1, L2, and L3 are parallel to ⟨010⟩ and have a low density of molecular kinks; hence, they have the slowest advance along [100]. In contrast, the upper parts have ledges that are oriented away from ⟨010⟩ and thus a higher density of kinks. These kinks advance by separation of molecules from the stack ends in the ⟨010⟩ direction. As a result, the protruding ledges in the upper parts of L1, L2, and L3 gradually disappear, leaving nearly straight ledges continuous with those in the lower part. Their movement then slows down to match that of the lower part. This ledge "straightening" effect is also seen in Figure 4 for L4 and L5 where the ledges become oriented in the ⟨010⟩ and ⟨100⟩ directions, respectively. Straightening can only occur if it leads to the formation of ledges of either ⟨010⟩ or ⟨100⟩ orientation with low index {100} or {010} ledge planes. Hence, because of the different rates of dissolution, the process proceeds toward the reduction of the number of kinks and of the surface energy.[13] Ledges of all other orientations have higher kink densities and move across the surface as a result of more rapid removal of molecules in the ⟨010⟩ direction from the ends of the stacks. As a result of the kink motion at ledges, the in situ ECSTM images of ledges of the TTF−TCNQ surface generally appeared frizzy (Figure 4). In this respect they resemble the results of STM observations from the electrochemical dissolution of monatomic steps of surfaces of metallic single crystals.[16]

The electrochemical reduction or oxidation of the crystal, as exemplified by Figure 8, also appears to follow the same pattern and to be determined by the density of molecular kinks and the rates of reactions at the kink sites, leading to straight ledges in the stack direction, ⟨010⟩, and their movement in the direction perpendicular to the stack. The orientation of ledges close to ⟨110⟩ in Figure 8c suggests the presence of a kink feature similar to that in Figure 5b and hence a high reactivity due to a high density of kinks. During the electrochemical reactions the surface undergoes not only dissolution of soluble products from the electrode surface but also the deposition of insoluble, and insulating, TTF^0 or $TCNQ^0$ on the surface. Detailed information at the microscopic scale about the possible effects of the formation on this new phase on the surface will be much more difficult to obtain and is a challenging subject for further investigation.
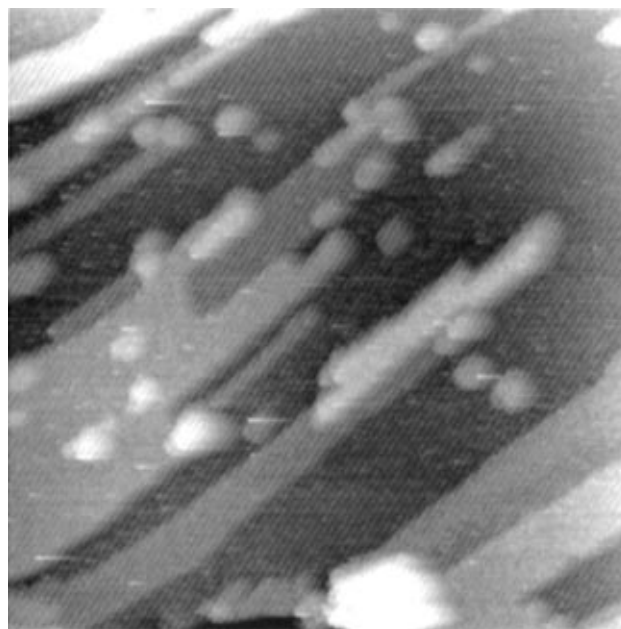

Figure 10. Height STM image (shaded) of the electrode surface obtained in air (500 × 500 nm, I_t = 0.5 nA, E_b = −200 mV, scan rate = 2 μm s^{-1}) following an in situ ECSTM experiment with dissolution at the equilibrium potential.

The present finding that the rate of dissolution is dependent on the orientation of the ledges with respect to the main crystallographic axes is consistent with previous studies of the growth and dissolution of other organic molecular crystals.[13] However, in the present work we have obtained for the first time direct dynamic evidence for the processes at the molecular level. The results of our dynamic imaging are consistent at the microscopic level with theoretical models of crystal growth and dissolution.[15] The anisotropy in the intermolecular bonding within these molecular crystals plays a key part in determining the dissolution mechanism,[13] and this is clearly evidenced in the present work. The strongest intermolecular bonding is along the molecular stacks due to strong overlap of the π orbitals and charge-transfer interactions between adjacent molecules within a stack.[9] The anisotropic dissolution and growth processes are also the reason for the formation of the natural macroscopic surface features found of these crystals[13] where the predominant steps run along a specific direction that is parallel to the molecular stack axis. Figure 10 is an image obtained in air after a separate in situ experiment and shows a general view of the electrode surface after dissolution at the equilibrium potential. The main steps are aligned parallel to the stack direction, and there are signs of the redeposition of material as hillocks at the end of molecular stacks, where the majority of kinks are located, favoring the nucleation and growth of material when local saturation exceeds a critical value.

Dissolution resulting from pitting may stem from lattice defects such as vacancies. The in situ image in Figure 11 shows examples of the type of vacancy (indicated by the arrowheads) observed at the TTF−TCNQ electrode surface due to molecules missing from a molecular stack. Only vacancies in the TCNQ stacks can be seen since the molecular detail is not well resolved for the TTF stacks. Similar molecular vacancies were also observed by STM in air for TTF−TCNQ[3] and BEDT−TTF[17] where they either were intrinsic lattice imperfections or arose because some molecules were removed by the tip during imaging. Surface vacancies with dangling charge-transfer bonds have been inferred to play a key role in the movement of surface ledges during the dissolution of (TMTSF)$_2$ClO$_4$ conducting crystals.[13] It is likely that similar effects occur in our case and that vacancy sites serve as centers for pit generation and growth.
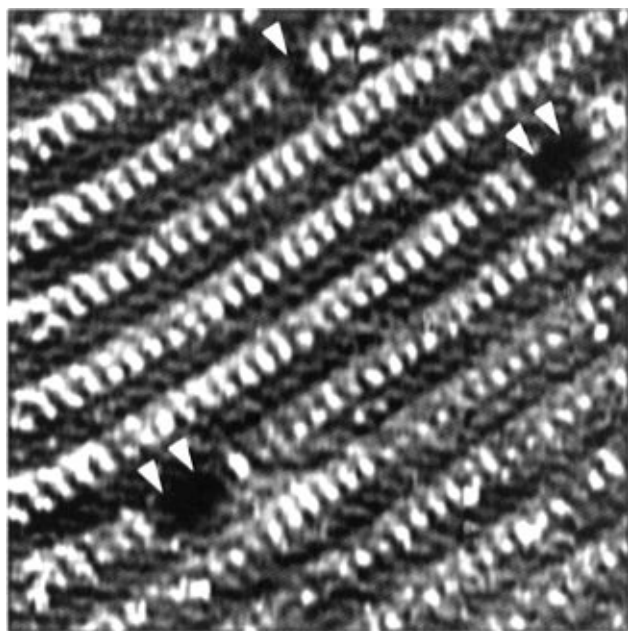
Figure 11. A 10×10 nm FFT low pass filtered current image of TTF−TCNQ molecular stacks showing molecular vacancies (marked by the arroheads), by in situ ECSTM in 0.01 M LiCl at the equilibrium potential and with $I_t = 1.5$ nA, $E_b = 100$ mV, and scan rate = 200 nm s^{-1}; a skewing of the image at the left-hand side of the frame with a brighter contrast is due to the nonlinearities of the scanner.

It is furthermore interesting to note that different pit morphologies can be observed on these crystals; compare the pits marked by P1 and P2 in Figures 4 and 7. In both cases these are shallow pits and hence can be inferred to originate from vacancy/impurity microdefects.[15] In a dislocation-free crystal, the shape of pits is known to be determined by the atomic structure of the lattice plane, and the boundaries of a pit correspond to close-packed lattice axes; hence, there is a coincidence between the pit symmetry and the symmetry of the crystal face.[15] Pits P1 and P2 in Figure 4 are rectangular and lie with their long axes along the stack direction. They are bounded by close-packed (100) and $(\bar{1}00)$ planes on the two long sides and by the ends of molecular stacks on the two short sides. Thus, they reflect the anisotropic stack nature of the (001) face. In contrast, pits P1 and P2 in Figure 7 are roughly triangular and are similar to larger scale (several micron) features seen on the surface of native crystals.[18] Once nucleated, both types of pit (as shown in Figures 4 and 7) grow by anisotropic dissolution.

The horizontal lines appearing in Figure 4 are an indication of species in motion, with the tip, along the scan direction; similar tip−substrate interactions have been observed in other in situ studies.[19] These horizontal lines were often observed in our in situ experiments regardless of the imaging conditions employed. This and other image noise are not unexpected since various solution species, including dissolved TTF and TCNQ and contaminants, are present in the electrochemical system. The fact that the horizontal lines do not appear in the STM images of the same crystals obtained in air (Figure 10) supports this interpretation.

The dissolution rate of TTF−TCNQ can be controlled by changing the electrode potential, as demonstrated in Figure 7. In this regard these crystals behave in the same way as metals[16] and other conducting organic salts.[13] However, in the case of TTF−TCNQ, because of the different possible reactions shown in eqs 1, 3, 6, and 7, the electrode can dissolve at all nonequilibrium potentials if the undersaturation induced by these reactions reaches a critical value. In other words, the electrode is only stable at the equilibrium potential in a saturated solution, provided that local saturation by TTF and TCNQ is maintained.
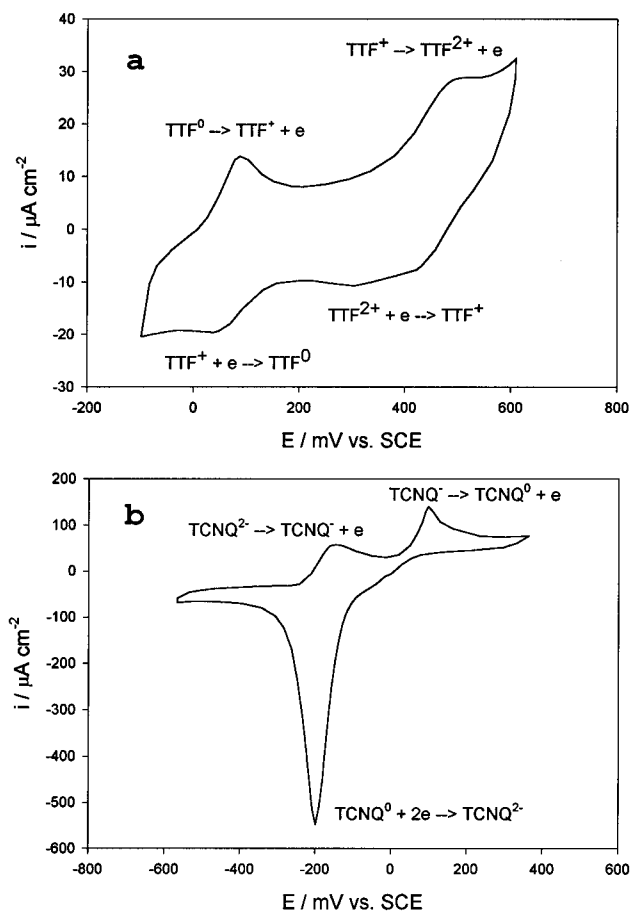

Figure 12. Cyclic voltammograms at Pt microelectrode (diameter 0.5 mm), with a Pt gauze counter electrode and a SCE reference, recorded at 20 mV s^{-1} in 0.01 M NaCl solution containing (a) 0.5 mM TTFCl and (b) 5 mM LiTCNQ. Note that the formation of insoluble TCNQ^0 on the anodic scan leads to subsequent stripping as TCNQ^{2-} on the following cathodic scan.

We cannot rule out the possible influence of faradaic reactions at the tip on the local saturation condition which may cause additional local dissolution during imaging. In fact, the extraordinary feature of fast dissolution seen in sequence 3 of Figure 7 can be explained in this way. Figure 12 shows cyclic voltammograms obtained with a Pt microelectrode in solutions of 0.5 mM TTF$^+$ or 5 mM TCNQ$^-$ in 0.01 M NaCl. For TTF (Figure 12a) we observe two one-electron redox processes corresponding to reduction of TTF$^+$ to TTF^0 at around 90 mV and oxidation to TTF^{2+} at about 490 mV. Thus, when the STM tip is held at 410 mV above an electrode at a potential positive of the equilibrium potential (that is, the conditions used to obtain sequence 3 of Figure 7), we can expect the tip to oxidize TTF$^+$ in solution in the vicinity of the tip during imaging. This will promote dissolution of the crystal by reaction 7 because it removes TTF$^+$ locally and thus increases the local undersaturation. This is a local effect which sweeps across the imaged area as the tip moves, and it is mainly lateral dissolution which is enhanced, resulting in a lateral dissolution rate that exceeds the vertical dissolution rate. This tip-enhanced dissolution process will be absent when E_t is reduced to 10 mV while keeping E_s unchanged, as illustrated by the fourth sequence of Figure 7. Now the dissolution rate is clearly reduced to the same level as, and with features similar to, that at the cathodic potential (sequence 1 in Figure 7).

TCNQ$^-$ also undergoes two one-electron reactions in aqueous solution (Figure 12b). In this case TCNQ$^-$ is reduced to TCNQ^{2-} at around -150 mV and oxidized to TCNQ^0 at around 100 mV. Thus, tip-induced effects due to faradaic reactions of TCNQ$^-$ are also possible. However, these are not significant

TTF−TCNQ Single-Crystal Electrodes

J. Phys. Chem. B, Vol. 101, No. 42, 1997 **8549**

in the case of sequence 3 in Figure 7 because TCNQ$^-$ is not expected to be a major dissolution product at this electrode potential where reaction 7 dominates. The results shown in Figure 7 highlight the importance of considering possible tip potential effects in the study of surface processes at organic conducting salt electrodes.

Conclusions

In situ electrochemical STM is a particularly useful technique for the study of single-crystal electrodes made from organic conducting salts. Using this technique, the structure of the electrode surface can be monitored dynamically in solution under potential control. At the same time, the surface molecular structure of the electrodes can be imaged at atomic resolution, so that anisotropy in electrode behavior can be directly correlated with the crystal structure and intermolecular bonding. In the present work we have successfully demonstrated this for the first time for dissolution processes at TTF−TCNQ single-crystal electrodes. In the future it may be possible to extend this approach to the study of the electrodeposition of these materials although this presents additional challenges since volatile organic solvents must be used.

Atomic resolution images of TTF−TCNQ from ECSTM at different potentials are identical with those expected from the bulk lattice structure and from STM in air, indicating that the surface structure does not depend on electrode potential. Dissolution of TTF−TCNQ in aqueous solutions can occur in several ways. Both anodic and cathodic overpotentials can produce undersaturation at the interface due to oxidation or reduction of the TTF and TCNQ components of the crystal. The dissolution kinetics are strongly dependent on the values of the overpotential. At small overpotentials, in the stable potential region where dissolution follows eqs 5, 6, or 7 the electrode surface generally dissolves both laterally and vertically at comparable rates with features typical of slow to medium rates of surface ledge motion with ledges separated by relatively large terraces. In contrast, at large overpotentials outside the stable potential range where two-electron process occur, reactions 1 and 3, the surface dissolves rapidly, producing narrow terraces marked by a large number of single and multiple ledges and accompanied by surface roughening and a reduction in the conductivity due to simultaneous deposition of insoluble, insulating reaction products. Other factors related solely to the instrumentation and technique can also play a part in affecting the interfacial dissolution processes. In particular, the tip itself can cause additional undersaturation as a result of faradaic reactions at the surface of the tip during STM imaging. In addition, temperature variations at the interface from instrumental sources can also promote dissolution even at the equilibrium potential in a saturated solution. These effects indicate some of the practical limitations of the in situ ECSTM technique—it is not necessarily a noninvasive probe of the surface reactions. Thus, care should be taken in the design of experimental protocol and in the interpretation of the results.

The important observation from our in situ ECSTM study is that for the first time the dissolution dynamics of these materials have been imaged at the molecular scale. The dissolution kinetics directly reflect the anisotropy of the TTF−TCNQ intermolecular bonding and the quasi-one-dimensional crystal structure. At the molecular level, the density of molecular kinks is directly related to the orientation of the ledge with respect to the crystallographic axes. Ledges of high index planes have a high density of molecular kinks. The molecules at these kink sites have dangling charge-transfer bonds and are thermodynamically less stable. Hence, they play a major part in the dissolution reactions. On the other hand, ledges orientated with low index, close-packed crystal planes, and in particular those oriented along the molecular stack direction, are the most stable and become the dominant surface features after dissolution. Dissolution occurs at a higher rate in the stack direction as a result of the dissolution of one molecule after another from the ends of the stacks. Microdefects caused by molecular vacancies within stacks are the probable origin of surface pits leading to gradual dissolution of the underlayers.

References and Notes

(1) Sleator, T.; Tycko, R. *Phys. Rev. Lett.* **1988**, *60*, 1418.

(2) (a) Magonov, S. N.; Bar, G.; Cantow, H.-J.; Ren, J.; Whangbo, M.-H. *Synth. Met.* **1994**, *62*, 159. (b) Magonov, S. N.; Whangbo, M.-H. *Adv. Mater.* **1994**, *6*, 355.

(3) Quivy, A.; Deltour, R.; van Bentum, P. J. M.; Gerritsen, J. W.; Jansen, A. G. M.; Wyder, P. *Surf. Sci.* **1995**, *325*, 185.

(4) (a) Schott, J. H.; Ward, M. D. *J. Am. Chem. Soc.* **1994**, *116*, 6806. (b) Schott, J. H.; Yip, C. M.; Ward, M. D. *Langmuir* **1995**, *11*, 177.

(5) (a) Yase, K.; Ara, N.; Kawazu, A. *Mol. Cryst. Liq. Cryst.* **1994**, *247*, 185. (b) Kato, N. A.; Yase, K.; Shigekawa, H.; Yoshimura, M.; Kawazu, A. *Synth. Met.* **1995**, *70*, 1245.

(6) (a) Kato, N. A.; Hara, M.; Sasabe, H.; Knoll, W. *Nanotechnology* **1996**, *7*, 122. (b) Kato, N. A.; Hara, M.; Knoll, W. *Mol. Cryst. Liq. Cryst.* **1996**, *280*, 211.

(7) (a) Jaeger, C. D.; Bard, A. J. *J. Am. Chem. Soc.* **1979**, *101*, 1690. (b) Jaeger, C. D.; Bard, A. J. *J. Am. Chem. Soc.* **1980**, *102*, 5435.

(8) (a) Albery, W. J.; Bartlett, P. N.; Cass, A. E. G. *Philos. Trans. R. Soc. London, Ser. B* **1987**, *316*, 107. (b) Bartlett, P. N. *J. Electroanal. Chem.* **1991**, *300*, 175. (c) Wilde, C. P.; Hu, A.; Rondeau, C. M.; Wood, M. *J. Electroanal. Chem.* **1993**, *353*, 19.

(9) Ward, M. D. In *Electroanalytical Chemistry*; Bard, A. J., Ed.; Marcel Dekker: New York, 1989; Vol. 16, pp 182−312 and references therein.

(10) Kaplan, M. L. *J. Cryst. Growth* **1976**, *33*, 161.

(11) Bartlett, P. N. In *Biosensors: A Practical Approach*; Cass, A. E. G., Ed.; IRL Press: Oxford, 1990; pp 47−95.

(12) Magonov, S. N.; Whangbo, M.-H. *Surface Analysis with STM and AFM: Experimental and Theoretical Aspects of Image Analysis*; VCH Press: Weinheim, 1996.

(13) Carter, P. W.; Hillier, A. C.; Ward, M. D. *J. Am. Chem. Soc.* **1994**, *116*, 944.

(14) Macpherson, J. V.; Unwin, P. R.; Hillier, A. C.; Bard, A. J. *J. Am. Chem. Soc.* **1996**, *118*, 6445.

(15) (a) Burton, W. K.; Cabrera, N.; Frank, F. C. *Philos. Trans. R. Soc. London* **1951**, *A243*, 299. (b) Heimann, R. B. In *Crystals: Growth, Properties and Applications*; Springer-Verlag: Berlin, 1982; pp 173−224 and references therein.

(16) (a) Suggs, D. W.; Bard, A. J. *J. Am. Chem. Soc.* **1994**, *116*, 10725. (b) Dietterle, M.; Will, T.; Kolb, D. M. *Surf. Sci.* **1995**, *327*, L495.

(17) Magonov, S. N.; Bar, G.; Cantow, H.-J.; Laukhin, V. N.; Yagubskii, E. B. *Synth. Met.* **1993**, *55−57*, 2222.

(18) The shape of the pits in Figure 7 is not the result of an imaging artifact caused by the fact that the dissolution rate is faster than the scan rate, an effect which has been identified in related AFM studies.[13] Comparing the dissolution rate and the scan rate of the imaging tip for Figure 4 and the second sequence of Figure 7, we can see that the dissolution rate in the latter appears slightly smaller than in the former, while the scan rate used for the latter is double that used for the former. The angular shape pits which we see in these images closely resemble numerous macroscopic angular recesses found on the *ab* surface of naturally formed TTF−TCNQ single crystals. They are all chevron with closely similar angles.

(19) Hendricks, S. A.; Kim, Y.-T.; Bard, A. J. *J. Electrochem. Soc.* **1992**, *139*, 2818.